Front. Chem. Sci. Eng. 2025, 19(9): 87
https://doi.org/10.1007/s11705-025-2600-z

REVIEW ARTICLE

Microstructural disorder in perovskite photovoltaics

Lifang Xie[1], **Yuanyuan Zhou** (✉)[1,2]

1 Department of Chemical and Biological Engineering, The Hong Kong University of Science and Technology, Hong Kong 999077, China
2 Energy Institute, The Hong Kong University of Science and Technology, Hong Kong 999077, China

Abstract Perovskites have emerged as promising semiconductors for solar cells and optoelectronics. Despite rapid advancements in device performance over the past decade, a quantitative investigation into structure-property relationships remains absent. The core of these innovations in fabrication lies in controlling long-range and short-range microstructural disorders in perovskites, yet their systematic impact across multiple spatial scales remains underexplored. In this review, we elaborate on hidden microstructural disorders, including interfacial disorders and intra-crystal disorders, further delving into their formation mechanisms and effects on mechanical reliability and long-term operational stability of perovskites. Unraveling these effects requires a combined approach of theoretical modeling and experimental characterization. Furthermore, we discuss theory-driven engineering strategies to mitigate such microstructural disorders, enabling the predictable processing and fabrication of stable and high-efficiency perovskite solar cells. This review aims to establish a foundational framework for transitioning from microstructure observation to microstructure control, which represents a critical frontier in the advancement of perovskite photovoltaics.

Keywords perovskite, microstructural disorder, photovoltaics

1 Introduction

Metal halide perovskites (MHPs) have emerged as a transformative class of materials in optoelectronics, driving advancements in photovoltaics, light-emitting diodes (LEDs), and photodetectors. Among these applications, perovskite solar cells (PSCs) have garnered particular attention, achieving certified power conversion efficiencies (PCEs) of over 27% in single-junction devices, which positions them as strong contenders for next-generation photovoltaic technology [1,2]. Unlike traditional semiconductors, MHPs accommodate a unique coupling between electronic and ionic charge carriers, allowing for unusual defect properties and enabling PSCs to maintain high performance despite structural heterogeneity [3–6]. As crystalline materials, MHPs are fundamentally governed by microstructural disorder, which manifests across multiple length scales, from atomic-scale lattice distortions to long-range structural heterogeneity [7,8]. This paradox underscores a critical scientific question: how and to what extent microstructural disorders influence the optoelectronic properties and stability of PSCs.

Over the past years, advances in processing techniques have led to significant improvements in the efficiency and stability of PSCs. To delve deeper, the essence of processing innovations lies in the regulation of microstructural disorder, which originates from the crystallization kinetics of solution-processed MHPs. Polycrystalline perovskite films, fundamental to PSC architectures, exhibit microstructure features such as grain boundaries (GBs) [9–14], heterointerfaces [15–22], and intra-crystal disorders (ICDs) [8,14,23,24], as illustrated in Fig. 1. GBs, the interfaces between adjacent grains, have historically dominated discussions on microstructural limitations in polycrystalline materials due to their impact on mechanical, thermal, and electrical properties [25,26]. In PSCs, GBs are often associated with high defect densities, acting as non-radiative recombination centers that reduce carrier lifetimes and device efficiency [27–29]. Under specific processing conditions, GBs can facilitate charge carrier separation or enhance local photovoltage and current generation [30–32]. Targeted passivation strategies have further rendered GBs electronically benign or even beneficial, mitigating recombination losses, and improving environmental stability [33]. Despite these advances, GBs remain critical pathways for ion migration, leading to compositional inhomogeneities, defect formation, and accelerated degradation under operational stress [34–36]. Such processes can trigger detrimental reactions with

Received March 25, 2025; accepted June 20, 2025; online July 31, 2025

E-mail: yyzhou@ust.hk

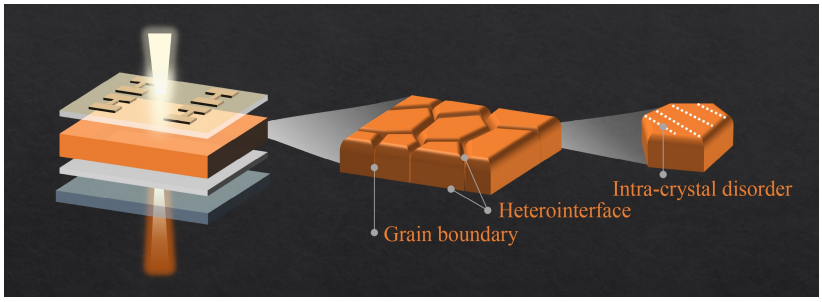

Fig. 1 The landscape of microstructural disorders in perovskite thin films encompasses GB, heterointerface, and ICD.

metal electrodes, such as silver, further compromising device longevity [37–39]. Due to their structural discontinuities and defect density, GBs are also vulnerable to decomposition under thermal stress, often serving as initiation sites for material degradation [40]. GBs have been the subject of considerable focus, but they represent only one facet of microstructural disorder, and their roles in thin films remain entangled with coexisting microstructure types. Heterointerfaces and ICDs remain relatively underexplored, due to limitations in available characterization techniques. Ignoring heterointerfaces and ICDs may lead to a misinterpretation of the role of GBs in MHP properties and PSC performance, potentially contributing to the current inconsistent insight of the microstructure-property-performance relationship [41]. Heterointerfaces are highly susceptible to intergranular cracking and delamination under operational stress, leading to efficiency losses and reduced device lifetimes. Recent advancements in heterointerface engineering have demonstrated its potential to address challenges such as ion migration, energy level misalignment, and defect passivation, contributing to significant improvements in efficiency and chemical stability [42–44]. However, the fundamental investigation on the mechanical reliability of heterointerfaces remains fragmented [43]. Similarly, ICDs, which influence intragrain charge transport and recombination, require further investigation to elucidate their role in device degradation fully. Their spatially localized yet pervasive nature complicates both their detection and mitigation, underscoring the need for improved probing methodologies and mechanistic insight.

This review summarizes current research on microstructural disorders at heterointerfaces and within intra-grain in determining the mechanical reliability and stability of PSCs. Furthermore, it explores their impacts, proposes mechanism-driven strategies to mitigate adverse effects of specific microstructural features. As research progresses, unlocking the precise role of microstructural disorder will be pivotal in realizing the full potential of PSCs for scalability and long-term durability.

2 Perovskite heterointerface

Heterointerface is not a singular, idealized boundary, but rather a statistical ensemble of individual contacts between perovskite grains and charge transport layers (CTLs). It is a pivotal area of investigation in device engineering, as it governs device performance by modulating charge transport and recombination. Historical efforts to enhance PSC performance and stability have centered on chemical modifications, leveraging strategies such as energy level alignment and surface defect passivation [45–51]. However, the mechanical reliability of heterointerfaces, an aspect shaped by their microstructure, has garnered comparatively little scrutiny. Interfacial delamination has emerged as a challenge under thermal stress, as device lifetimes become increasingly important, necessitating robust mechanical adhesion to mitigate degradation reactions [52,53]. In typical *n-i-p* device configurations, the buried heterointerface, typically formed between the perovskite layer and the underlying electron transport layer (ETL), has received less attention than the more accessible top interface, perovskite/hole transport layer (HTL), where passivation using organic species such as Lewis acid/base compounds and polymers has been widely explored [54–57]. Environmental stressors such as heat or illumination often exacerbate these issues, triggering volumetric expansion of interfacial voids and accelerating performance degradation [58–60]. Additionally, the intrinsic roughness and high defect densities, such as metal vacancies and hydroxyl groups, in widely used n-type metal oxide ETLs (e.g., SnO_2, TiO_2, ZnO) further deteriorate interface quality [60]. For instance, the surface roughness of TiO_2 has been directly linked to perovskite grain morphology and overall device efficiency [61]. Current strategies to reinforce interfacial bonding often rely on molecular "interfacial glues" that enhance chemical interactions at the perovskite interface [43,52]. These methods tacitly presume a flat, continuous interfacial microstructure. In reality, thermodynamic forces drive the formation of complex interfacial geometries, including grain boundary grooves (GBGs) and grain surface concavities (GSCs). Even minor flaws at the interface can weaken interfacial adhesion, leading to delamination under environmental stress. These microstructural traits cumulatively degrade mechanical reliability and long-term stability of PSCs. This section examines the formation mechanisms of these morphological features,

their detrimental effects, and potential strategies to mitigate their adverse impacts.

2.1 GBG

Perovskite thin films are typically polycrystalline structures with GBs forming a three-dimensional (3D) network [62]. GB properties, such as density, distribution, and misorientation angles, have been shown to significantly influence the PSCs' performance [33]. GBs are often modeled conventionally as directly intersecting surface heterointerfaces (as shown in Fig. 2(a)), but this oversimplification neglects the energetic instability of such flat exposed surfaces [63]. The dynamics of GBG formation can be quantitatively explained through thermodynamic principles. In the ideal initial state, where the dihedral angle (φ = 180°), stress and energy imbalances at the intersection of the surface and GB network drive structural evolution during annealing to minimize the total Gibbs free energy [62]. When adjacent grains meet and align along distinct crystallographic orientations, this energy minimization facilitates material transport from GB to grain surfaces, promoting the formation of GB channels and coupled ridges in adjacent regions, thereby reducing stress from surface and GB energy disparities [63,64]. These GBGs, depicted in Fig. 2(a), form at the perovskite-substrate heterointerface through solid-state ion diffusion. Based on the energy-driven groove formation theory, the side angle of the groove, θ, is determined by the ratio of GB energy (γ_{GB}) to surface energy (γ_s). This relationship provides a quantitative framework for characterizing the morphology of GBGs and their impact on PSC performance.

The formation of GBGs has multifaceted impacts on device performance and stability. These grooves disrupt charge transport and compromise chemical stability; more critically, as a structural crack, they serve as a potential initiation site for mechanical delamination at the heterointerface [20]. These impacts can be categorized as follows, as illustrated in Fig. 2(d): (1) GBGs introduce 3D nanovoids, which disrupt the continuity of charge transport pathways. These voids act as barriers to efficient electronic conduction. (2) 3D nanovoids act as traps for moisture or solvents, accelerating material degradation [65]. High surface ionic reactivity near GBGs promotes the migration of ions [12,66], leading to structural volume changes such as groove expansion and the formation of bubble-like features at heterointerfaces,

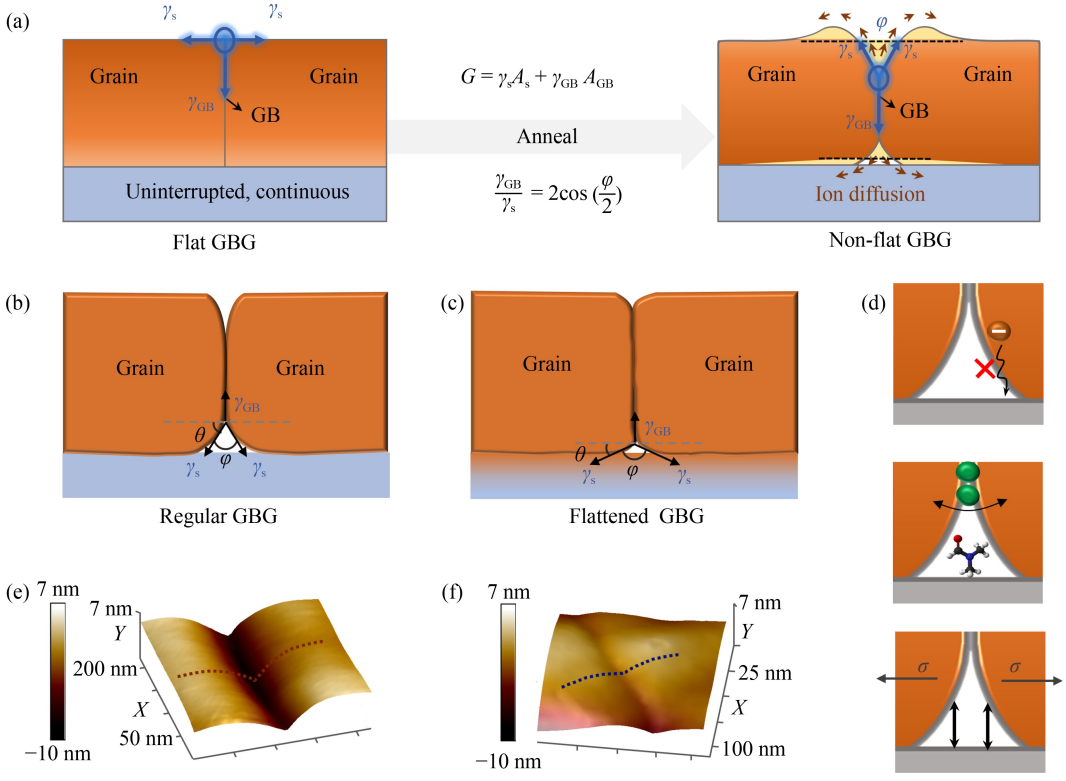

Fig. 2 Schematic representations of GBGs at perovskite-substrate heterointerface. (a) Thermodynamic evolution of GBGs, where G and δG are total Gibbs free energy and corresponding changes; γ_{GB} and γ_s represent GB energy and surface energy; A_{GB} and A_S are the area of the GB and surface, respectively; φ and θ represent the dihedral angle and the side angle of the GBG, respectively. (b) and (c) regular and flattened GBG microstructures. (d) GBG's negative impacts include obstructing charge transport across the heterointerface, reducing chemical stability by promoting ion migration and trapping moisture or solvents, and weakening mechanical integrity, leading to interfacial delamination. Reprinted with permission from Ref. [20], copyright 2024, Elsevier. (e) and (f) high-resolution 3D atomic force microscopy (AFM) images of regular and flattened GBGs. Reprinted with permission from Ref. [21], copyright 2023, Wiley.

further exacerbating device degradation. (3) GBGs serve as natural edges for interfacial delamination under mechanical or environmental stresses. A mismatch in thermal expansion coefficients between perovskites and adjacent layers induces thermally driven tensile strain at the heterointerface [67,68]. This strain concentrates at GBG locations, leading to interfacial sliding and undermining the mechanical integrity of the perovskite-substrate interface. Over time, these stresses cause void formation, groove deepening, and widening near GBG-adjacent regions, further weakening the interface. Therefore, flatter grooves can reduce stress accumulation, prevent delamination, and maintain morphological stability under stress.

To eliminate the detrimental effects of GBGs, strategies focusing on GB energy tuning have proven effective. The balance between γ_{GB} and γ_s can be effectively modulated through chemical additives, either introduced into the precursor or embedded within the CTL, which alter γ_s and γ_{GB} through ionic redistribution during annealing. An example is the widely adopted glass/ITO/SnO_2/$FA_{0.9}Cs_{0.1}PbI_3$/PMMA/epoxy/glass device stack, in which GBGs at the buried interface are primarily dictated by γ_s, which can be tuned via volatile additives [20]. Isobutylammonium chloride (i-BACl), a volatile organic salt, coats on SnO_2 surface and has been shown to migrate toward the perovskite/ETL interface during high-temperature annealing. This migration alters the local heterointerfacial energy landscape and reshapes the GBG geometry. First-principles calculations reveal that i-BACl modification increases the relative heterointerfacial energy from 0 to 1.4 eV·nm^{-2}, leading to a significant reduction in GBG side angle θ, as illustrated in Fig. 2(c) [21]. High-resolution AFM has confirmed this "flattening" effect, revealing significant improvements in interface contact and reduced groove depth. Before and after modification, noticeable reductions in groove side angles enhanced the contact between the perovskite and CTL, as shown in Figs. 2(e) and 2(f). Correspondingly, partial incorporation of FACl into i-BACl leads to measurable changes in GBG morphology, producing a mean GBG side angle of 9°, in agreement with the trend in calculated heterointerface energies for different organic cations [21]. In parallel, tuning γ_{GB} through precursor solution additives provides another practical pathway to control GBG morphology. Additives influencing crystallization kinetics further promote groove side angle reduction and morphological uniformity by redistributing interfacial energy [12]. The concurrent optimization of γ_s and γ_{GB} for tailoring GBG geometry minimizes stress concentrations at the heterointerface, promoting more uniform GB alignment. On the device level, such improvements manifest as an increase in mechanical reliability and prolonged operational lifetime, underscoring the vital role of interfacial energy regulation in advancing PSC stability and performance.

2.2 Nanoscale groove traps (nano-GTs)

Nano-GTs can spontaneously form at triple junctions of grains in polycrystalline thin films, as shown in Fig. 3(a). During annealing crystallization, the thermodynamic competition between GBs and the free surface drives energy relaxation. According to the thermally driven groove theory, the high GB energy at triple junctions promotes surface atom rearrangement via surface diffusion, forming a complex 3D "wormhole-like" structure to minimize the system's total energy [69,70]. This process follows the thermodynamic extremum principle, wherein the system tends toward a steady-state geometry that balances surface curvature and GB energy. When three grains intersect, their orientation mismatches induce localized stress concentrations and lattice distortions, and further the groove root extends into the grain interior. Ultimately, the total depth of nano-GTs (d_{GT}) arises from the superposition of the GBG depth (d_G) and groove root depth (d_{GR}).

The interplay between microstructure, compositional uniformity, and macroscopic device performance is intrinsically linked. Microstructural defects impede the uniform distribution of cations from the nanoscale to the macroscale. Out-of-plane compositional heterogeneity across the entire film has been visualized in detail [71], and in-plane cation inhomogeneity has been observed with strategies developed to mitigate it [72]. Nonetheless, controlling nanoscale intergranular cation disparities remains challenging. Due to the intrinsic microstructure of the GB network, in addition to the previously discussed GBGs, nano-GTs exert a significant influence on cation diffusion dynamics in formamidinium-caesium (FA-Cs) perovskite films [73], as shown in Fig. 3(b). These groove structures, which naturally accumulate at GBs in a polycrystalline matrix, act as physical barriers that hinder thermally driven cation diffusion between adjacent grains. Specifically, d_{GT} governs cation homogeneity in $FA_xCs_{1-x}PbI_3$ films. As shown in Figs. 3(b) and 3(d), when d_{GT} exceeds 10 nm, its strong spatial hindrance traps diffusing cations and obstructs cross-grain mixing, thereby exacerbating compositional differences and leading to nanoscale heterogeneous regions. This topologically induced inhomogeneity causes $FA_xCs_{1-x}PbI_3$ films to deviate from the ideal phase purity, as evidenced by altered exciton dynamics in cathodoluminescence mapping. Consequently, carrier mobility is reduced, nonradiative interfacial recombination intensifies, and devices with deep traps exhibit lower PCEs compared to their optimized counterparts [73].

The geometry of nano-GTs is governed by the line tension balance at grain boundary triple junctions [73–76], as shown in Fig. 3(c). The ζ between the groove root and the film plane is determined by the balance between the groove-root interfacial line tension (γ_{IS}) and the triple-line tension (γ_{TL}). Given that solid-state cation

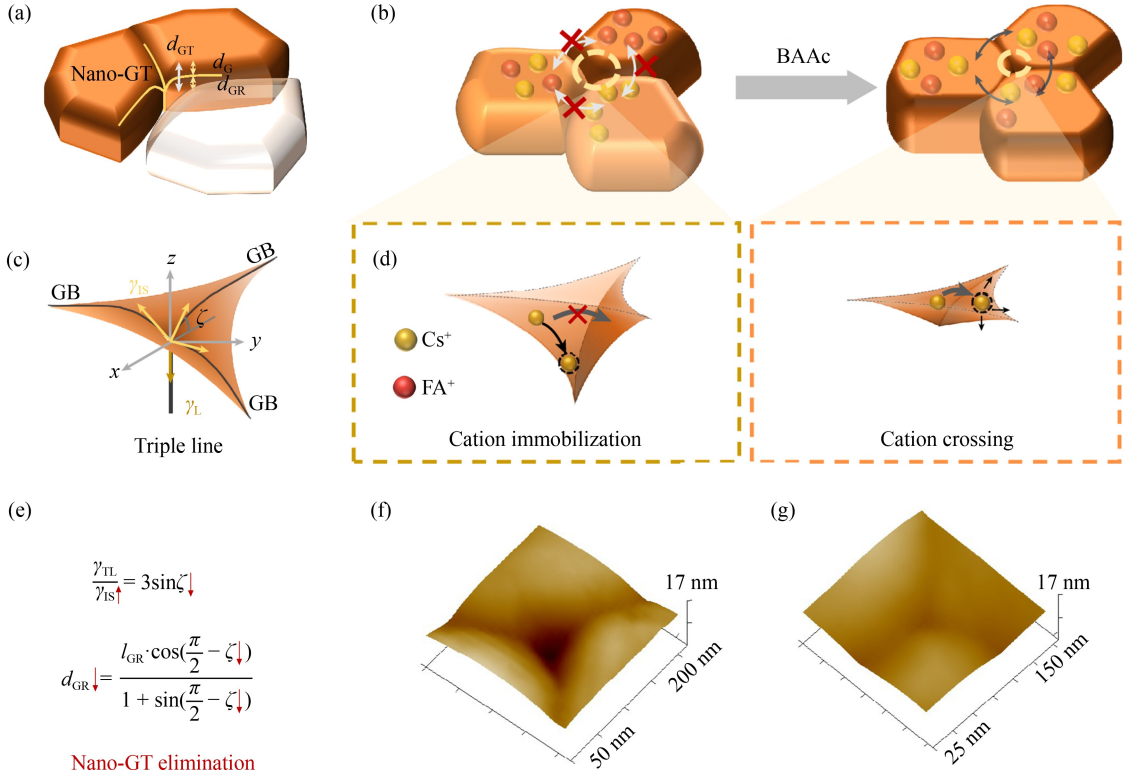

Fig. 3 Schematic illustration and mitigation strategies for nano-GTs at perovskite-substrate heterointerface. (a) 3D representation of a nano-GT in a perovskite film, where d_{GT}, d_G, and d_{GR} denote the depths of the nano-GT, GBGs, and groove root, respectively. (b) Influence of nano-GT depth on cation homogeneity in FA-Cs perovskite films, comparing deep and shallower nano-GTs (BAAc: butylammonium acetate). (c) Line tension equilibrium and energy distribution at nano-GTs, where γ_{IS} and γ_{TL} represent the groove root line tension energy and the triple line tension energy, respectively. The characteristic angle (ζ) indicates the angle between the groove root and the horizontal film plane. (d) Illustration of cation immobilization within nano-GTs acting as geometric traps, compared to cation diffusion across shallowed nano-GTs. (e) Nano-GT elimination strategy based on mathematical formulation, where l_{GR} represents the projected groove length in the vertical direction. (f) and (g) AFM images showcasing nano-GTs in (f) pristine and (g) shallowed nano-GTs. Reprinted with permission from Ref. [73], copyright 2025, Nature.

diffusion predominantly occurs along polycrystalline surfaces [77], theoretical analysis indicates that reducing ζ, a shallowing effect primarily driven by γ_{IS}, can significantly decrease d_{GT}. Mathematical formulations are illustrated in Fig. 3(e). Guided by these insights, a volatile additive, BAAc, was introduced to modulate the perovskite γ_s to 1.068 eV·nm^{-2}, compared to 0 eV·nm^{-2} for the pristine interface. Both the BA^+ cation and Ac^- anion contribute to surface energy modulation at the buried interface: BA^+ interacts with the perovskite via anchoring mechanisms, whereas Ac^- substitutes into the lattice, inducing more pronounced compressive strain and thereby elevating γ_s more significantly [78–80]. From a structural standpoint, Ac^- incorporation introduces lattice distortion that serves as the underlying origin of the interfacial energy increase, ultimately governing interfacial geometry. An increase in γ_s leads to a corresponding rise in γ_{IS} within nano-GTs due to their positive correlation, thereby disrupting the original line tension balance and inducing a shallowing of the nano-GTs. During annealing, BAAc is released from the ETL and acts at the perovskite/substrate interface, reducing the average nano-GT depth at the film bottom from 15.3 nm (control, Fig. 3(f)) to 4.4 nm (treated, Fig. 3(g)), thus achieving a shallow trap structure. This geometric modulation effectively alleviates the cation diffusion barrier at GBs and promotes FA^+–Cs^+ cross-grain exchange [73]. These findings suggest a promising direction for designing optimized additives that pair bulky organic cations with pseudo-halide anions to precisely tailor nano-GT geometry.

A quantitative relationship among microstructure, line tension regulation, and cation homogenization can provide critical guidance for perovskite interface engineering. Cation inhomogeneity between grains induces conduction band minimum (CBM) fluctuations while valence band maximum (VBM) remains stable, and shallower nano-GTs promote energy level alignment across grain surfaces, reducing these variations [73,81]. Photoluminescence (PL) and time-resolved PL measurements further confirm that shallowed nano-GTs reduce nonradiative recombination losses and accelerate carrier injection dynamics. The resultant lateral cation homogenization yields nearly ideal perovskite grains with compositions that closely adhere to the ideal stoichiometry and Goldschmidt tolerance factor, ensuring enhanced phase

stability under operational conditions. Mechanistically, optimizing interfacial chemical uniformity through crystallization kinetics modulation effectively reduces localized lattice strain and ion migration driving forces, aligning with established understanding of perovskite intrinsic stability. This methodology demonstrates broad applicability across mixed-cation/halide perovskite systems, where improved uniformity of metal cations and halide anions proves critical for developing stable perovskite/silicon tandem solar cells [82].

2.3 GSCs

Void formation at the buried interface of the hidden bottom layer in PSC is a critical phenomenon during the initiation of crystallization, ranging from tens or hundreds of nanometers to micrometers in size [83–87]. These voids arise due to various factors, including GB-induced effects and solvent trapping [65]. Because standard annealing temperatures (< 150 °C) lie below the dimethyl sulfoxide (DMSO) boiling point, crystallization begins at the film/air surface, generating a rapid shell that allows ≈ 90% of the DMSO to escape while trapping the remaining ≈ 10% within an intermediate phase [88]. Over extended annealing, the residual DMSO eventually evaporates from the maturing crystal lattice, causing local volumetric collapse and void formation predominantly near the buried contact layer. Hence, methods that accelerate solvent extraction (vacuum-flash, hot-gas quenching) or weaken coordination (Lewis-acid scavengers, volatile co-solvents) markedly suppress void formation. However, GSCs-induced nanogaps are fundamentally different from voids generated by GBGs or by random solvent trapping at heterointerfaces [21,65,85–87]. GB-induced voids are typically confined to lateral extensions of only a few tens of nanometers along the bottom interface, and solvent-trapping voids are typically random, forming isolated micro- or macro-scale cavities that localize near the heterointerface [65,89]. In contrast, nanogaps induced by GSCs can span entire grains, making them a dominant structural feature in large-grain perovskite films [22]. Importantly, their formation mechanism is also distinct. This distinction in both geometric scale and origin underscores the need to treat GSCs as a unique and structurally impactful class of defects in buried heterointerface engineering. GSCs are defined by the inclination of the line connecting the ridge peak and the concavity center relative to the horizontal plane, in conjunction with GBG. The formation and evolution of GSCs are closely linked to thermodynamic processes, as depicted in Fig. 4(a). During solution-based grain growth, biaxial tensile strain (BTS) arises from interatomic forces at GB, leading to lateral deformation (ε_{xy}) [90]. Through the Poisson effect, this lateral strain is converted into out-of-plane deformation (ε_z), which manifests as concavities at the grain centers. Simultaneously, thermal grooving occurs during the annealing process, further shaping GSCs. Thermally driven ion migration redistributes solid-state ions from GBs toward grain edges, forming convex ridges and accentuating concavities at the grain centers. This redistribution is driven by thermodynamic considerations that minimize the total energy of the grain structure. Together, these processes, strain-induced deformation and thermal grooving, alter the topography of perovskite grains, producing GSCs that significantly impact the morphology and mechanical reliability at the heterointerface.

To mitigate the adverse effects of GSCs, a promising approach involves tailoring the surface and GB energies to suppress GSC formation. As shown in Fig. 4(c), GSC elimination process can be modeled through the grain-coalescence-induced BTS formula. Specifically, minimizing BTS by reducing $(2\gamma_s - \gamma_{GB})^{0.5}$ can effectively decrease the ε_{z_BTS} caused by GSCs [22]. One effective strategy for achieving this goal is the use of fluorinated surfactants like TFSAP, as shown in Fig. 4(b). Its sulfo group anchors at iodide vacancies on the perovskite surface and GBs, while the electron-rich, all-fluorinated tail prevents self-aggregation. These interactions enable TFSAP to homogeneously distribute along grain micro-surfaces, lowering both γ_s, γ_{GB}, and their difference, further flattening GSC geometries. Importantly, the improvement in mechanical integrity arises from the cumulative elimination of interfacial concavities, enabling better grain-ETL contact across the film. The same rationale extends to other additives with complementary anchor groups and hydrophobic backbones, like Pluronic P123 and *N*,*N*,*N*-trimethyloctan-1-aminium chloride, both of which relax BTS and eliminate GSCs through interfacial-energy tuning. By contrast, molecules lacking a sufficiently long fluorinated segment, such as potassium trifluoromethanesulfonate, show negligible influence on GSC geometry at comparable loadings despite having similar sulfonic headgroups and molecular-scale passivation effects [91,92]. Hence, the observed benefits of TFSAP are primarily attributed to geometric regulation of the GSCs rather than to molecular-scale chemical passivation. Collectively, these results highlight a general additive-design with molecules that incorporate hard-base anchor groups and rigid hydrophobic chains. Additionally, the molecular structure of TFSAP inhibits the diffusion of solid-state ions during the annealing process, effectively suppressing thermal grooving and, consequently, minimizing the formation of GSCs. AFM images provide clear evidence of these improvements. As shown in Figs. 4(d)–4(g), two-dimensional (2D) and 3D scans reveal detailed local geometric features across adjacent grain. For untreated films, the grains exhibit concave center surfaces surrounded by convex ridges and GBGs. In contrast, the target films treated with TFSAP show nearly flat grain surfaces with minimal GSC

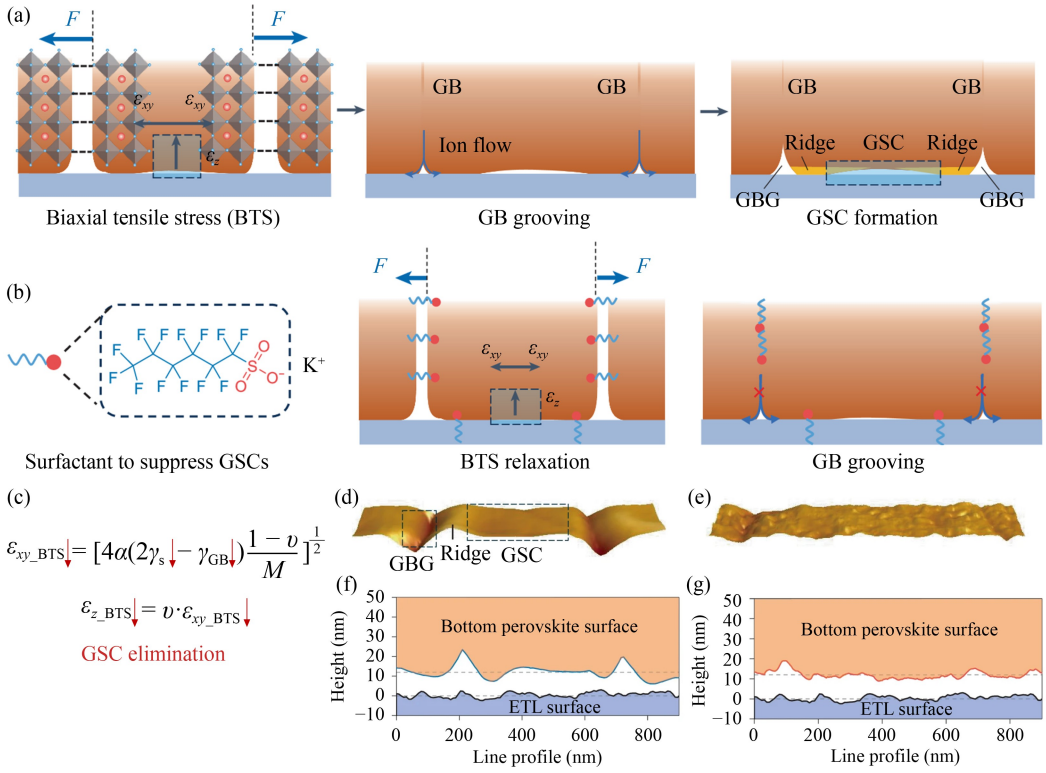

Fig. 4 Formation mechanisms and mitigation strategies of GSCs at perovskite-substrate heterointerface. (a) The thermodynamic evolution of GSCs. Bonding-induced biaxial force (F) induces lateral deformation (ε_{xy}), which leads to out-of-plane deformation (ε_z) via the Poisson effect. Ion diffusion from grooves to ridges drives the formation of GSCs and convex ridges. (b) Tridecafluoro-hexane-1-sulfonic acid potassium (TFSAP) strategy to reduce ε_{z_BTS} by altering surface and GB energies and suppressing ion diffusion, ultimately minimizing GSC formation. (c) GSC elimination based on grain-coalescence-induced BTS formula, where a is half of the grain size, γ_s is the surface free energy per unit area, γ_{GB} is the GB energy per unit area, M is the Young's modulus and v is the Poisson's ratio. (d) and (e) 3D AFM images of perovskite film surfaces with and without GSCs. (f) and (g) 2D height profiles reveal nanovoids at interfaces with GSCs, contrasting with the smooth integrity of films without GSCs. Reprinted with permission from Ref. [22], copyright 2024, Nature.

formation. This improvement in grain surface morphology leads to a more uniform interface between the perovskite and the CTL. It has been proven to enhance mechanical strength and device stability under various stress conditions [22]. This structure-function strategy enables *in situ* tuning of interfacial energies and offers a promising route to optimize perovskite film morphology and device stability.

The mechanical reliability of heterointerfaces can be assessed using the ASTM D3359 tape test, a widely adopted method for evaluating the adhesion reliability between thin films and substrates, as illustrated in Fig. 5(a). The statistical distributions of normalized delaminated area (Fig. 5(b)) and interfacial adhesion strength (Fig. 5(c)) can serve as key metrics for evaluation. Standardized testing reveals that films with GSC elimination exhibit stronger adhesion. The overall improvement in mechanical reliability can be attributed to the accumulation of optimized micro-heterointerfaces. Additionally, the advantages of non-concave grains can be further amplified using interface molecular adhesives. One effective strategy involves employing iodine-terminated self-assembled monolayers (I-SAM) as an adhesive between the perovskite grains and CTL. Minimizing GSCs increases the interfacial contact area, facilitating the formation of more hydrogen bonds through the incorporation of SAM. The microstructure flattening approach enhances the mechanical strength of perovskite devices and further amplifies the benefits of existing SAM-based interface engineering.

Similar to the adverse effects of GBGs, GSCs introduce nanoscale voids at the heterointerface that exacerbate device instability. Regarding environmental resistance, GSCs affect long-term stability under stressors such as temperature fluctuations, humidity, and light-induced degradation. The concave geometry of GSCs acts as reservoirs for moisture and solvent infiltration, accelerating material degradation. Under damp-heat conditions (as shown in Fig. 5(e)), GSCs promote water accumulation at the micro-heterointerface, obstruct thermal transfer, and create localized hotspots. This combination of trapped moisture and heat accelerates the degradation of the micro-heterointerface, leading to further structural deterioration. Mechanically, GSCs act as stress concentrators, becoming weak points prone to interfacial delamination under thermal cycling stress. As

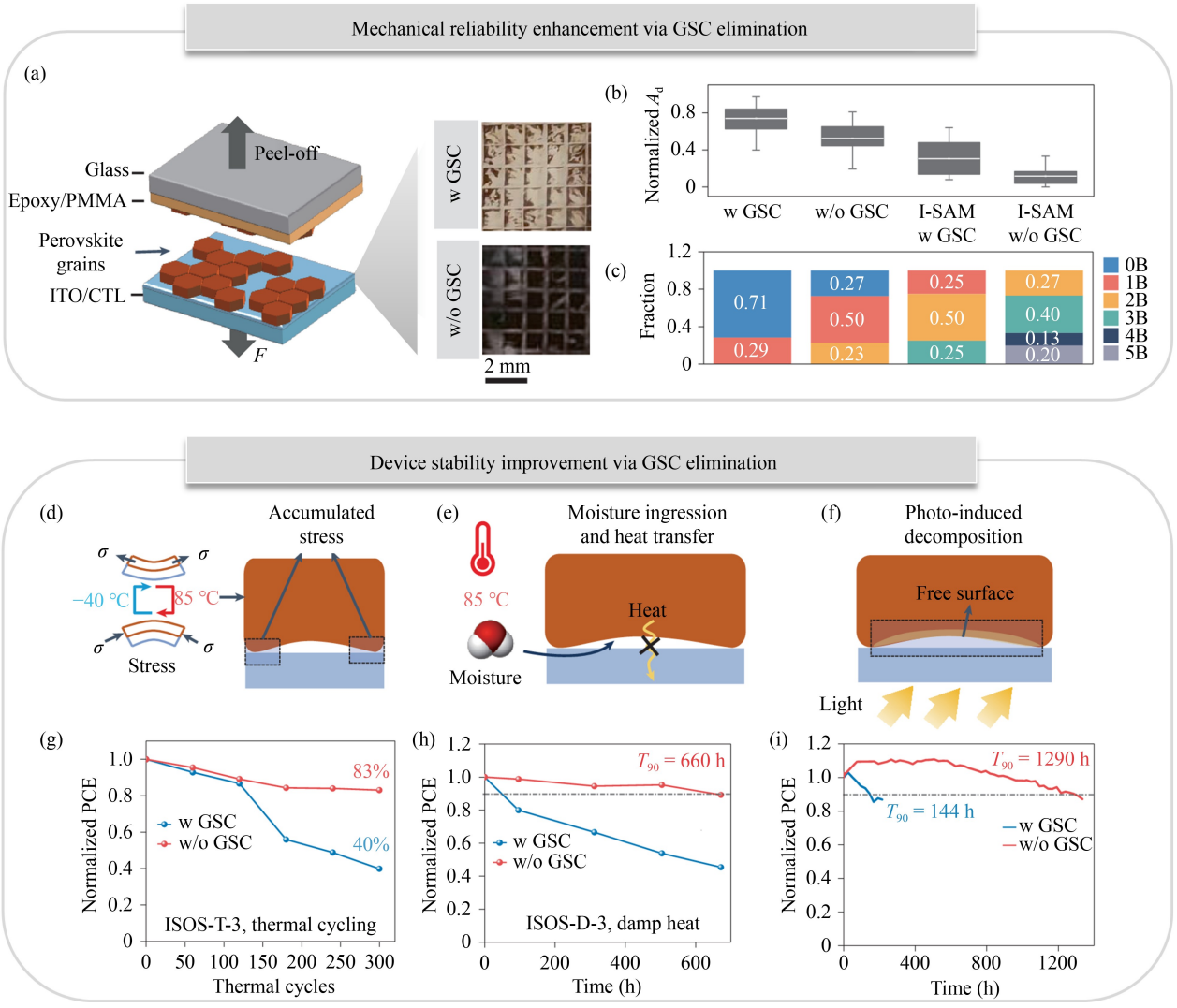

Fig. 5 Enhancement of mechanical reliability, device performance, and durability through GSC elimination. (a) Schematic illustration of the delamination process for quantitative assessment of the perovskite-CTL heterointerface mechanical reliability. (b) Statistical distribution of normalized delamination area and (c) interfacial adhesion strength (0B–5B) based on ASTM D3359 standard, where higher numbers indicate stronger interfacial strength. (d) Strain evolution during thermal cycling, with GSCs inducing interfacial delamination due to accumulated stress on convex ridges. (e) GSCs promote moisture ingress and hinder heat dissipation, causing moisture and heat accumulation at the micro-heterointerface. (f) Photothermal decomposition at exposed GSC surfaces. (g)–(i) Comparative durability of PSCs with and without GSCs: (g) thermal cycling durability, (h) damp heat durability, and (i) maximum power point (MPP) stability. Reprinted with permission from Ref. [22], copyright 2024, Nature.

illustrated in Fig. 5(d), thermal cycling causes cyclic compressive and tensile strain due to mismatched thermal expansion coefficients between grains and CTL. This thermal stress accumulates at GSC locations, promoting delamination at convex ridges and weakening the overall structural robustness. Additionally, GSC-exposed surfaces are highly susceptible to photothermal decomposition during prolonged light exposure, as shown in Fig. 5(f). These concavities ultimately shorten the operational lifetime of perovskite devices. However, based on the discussed TFSAP strategy to mitigate GSCs, Figs. 5(g)–5(i) confirm that eliminating GSCs has a significant positive impact on the thermal-cycling durability, damp-heat durability, and MPP stability of perovskite devices.

Thermodynamic energy-based engineering strategies offer a robust pathway to overcoming the mechanical and chemical limitations of polycrystalline perovskite films. Because microstructural disorders often coexist and interact, establishing a strict hierarchy among them is impractical. Instead, achieving optimal device performance requires a holistic approach: suppressing nano-GTs helps local compositional purity, smoothing GSCs facilitates efficient carrier extraction, and flattening GBGs enhances interfacial adhesion and mechanical durability. Table 1 summarizes current strategies for modulating interfacial energetics and morphology at the buried perovskite heterointerface. Interfacial-energy modulators, including alkylammonium salts, carboxylates,

Table 1 Modification strategies for microstructural control at perovskite heterointerface

Chemical class	Representative formulation	Influencing parameters	Target	Microstructure impact	Device improvement	Ref.
Alkyl-ammonium salt	i-BACl pre-buried in SnO_2	Raises surface energy (γ_s)	GBGs	Mean GBG side-angle reduce from 11.01° to 7.56°; nanovoids suppressed	Mechanical reliability increases; PCE retentions increase under damp/heat test	[21]
Carboxylate	BAAc pre-buried from SnO_2	Increases groove root line tension (γ_{IS})	Nano-groove traps	Trap depth d_{GT} drops 15 → 4 nm	PCE 25.6%; 90% retention after 1000 h	[73]
Anionic surfactant	TFSAP in precursor	Lowers γ_s and γ_{GB}; hinders surface ion flow	GSCs & GBGs	Concavity angle ξ drops 2.1° → 0.5°; θ_{GBG} 15.9° → 9.9°	90% PCE retention in device stability tests	[22]
SAM	C_{18}-PA SAM on ITO	Crystalline SAM smooths perovskite bottom	GB-induced ridges at bottom	Flatter buried surface	PCE 19%; 90% retention after 1400 h	[110]
Heterocyclic Lewis base	1H-1,2,4-triazole in FA-based ink	Pb-N & H-bonding slow nucleation	GBs during crystallization	Larger, monolithic grains; GB density markedly reduces	1 cm^2 cell PCE = 23.1%; 94% PCE retention, 1000 h @65% RH, 45 °C	[93]
Lewis-base solvent	DMF:DMSO:NMP (4:0.75:0.25) solvent of precursor	Strong PbI_2-NMP binding → slower growth	DMSO-induced nanovoids	Grain size increases; void density markedly decreases	PCE of PSC from 17.0% to 21.5%	[111]
Non-volatile Lewis base	Carbohydrazide (CBH) in solvent	Remains during anneal; prevents volume collapse	Bottom-region shrinkage voids	Void-free, dense buried interface	< 1% PCE loss after 550 h @60 °C	[89]
Lewis-base additive	4,4′-dinonyl-2,2′-dipyridine (DN-DP) in CB antisolvent	Replaces DMSO; slows crystallization	Volume-collapse voids (SnO_2 side)	Surface roughness Rq reduces from 30.1 to 15.9 nm; voids at SnO_2 interface reduce	90% PCE retention after 1000 h of storage	[94]
Lewis-base additive	CBH in solvent	Pb-carbonyl coordination slows nucleation	Voids in buried perovskite interface	> 90% suppression of ~100 nm voids	< 1% loss after 550 h MPP; blade-coated mini-modules 20.1% (17.9 cm^2)	[89]
π-bridged small molecule	TAPT interlayer	H-π bonding to PTAA and π-Pb^{2+} coordination passivate defects and delay crystallization	Micro-cracks in PTAA/perovskite buried interface	Compact interface; enlarge grains; suppress GB micro-cracks	89.7% retain after 1500 h MPP; 91.9% after 1065 h at 85 °C	[96]
Large organic cation	F-PEAI dual-interface modification (HTL pre-wash + antisolvent)	Raise PTAA surface energy, improve wettability; residual cation passivates both interfaces	Nanovoids in PTAA/perovskite bottom and perovskite/PCBM top	Elimination of nanovoids; smoother top surface	≈ 100% of initial PCE preserved over 2100 min of continuous light	[98]
Amphiphilic bifunctional SAM	MPA-CPA bilayer spin-cast on ITO	Super-wetting over-layer lowers contact angle for uniform nucleation; cyano-phosphonate binds Pb/O to suppress interfacial traps	Nanovoids and defective contact at perovskite/ITO interface	Void-free, tight contact	Certified PCE 25.4% with V_{OC} 1.21 V, FF 84.7%	[95]
Formate inter-layer	FAFa dip-coated on SnO_2	$HCOO^-$-mediated oriented recrystallization	Pinholes/voids at SnO_2-perovskite buried interface	Pinhole density decreases; RMS roughness reduces from 11.3 to 7.3 nm	PCE 23.5% with improved storage stability and photostability	[83]
Multiply-charged conjugated polyelectrolyte	MPS-TMA interlayer on PTAA	Ionic side-chains make PTAA hydrophilic and serve as nucleation sites; TMA^+ passivates interfacial traps	Nanoscale pinholes and poor wetting at PTAA/perovskite interface	Compact, void-free coverage with more uniform grains	1 cm^2 cell: PCE 18.94%	[97]

and fluorinated surfactants, can selectively reduce γ_s and γ_{GB}. This leads to suppressed voids, flattened heterointerface, and improved damp-heat stability. Precursor coordination additives (e.g., Lewis bases) delay crystallization or displace solvents like DMSO, enlarging grains and preventing buried void formation [89,93,94]. Formamidine formate (FAFa) modulates interfacial energy or relieves lattice strain to heal pinholes and flatten buried topography [83]. On HTL side, surface modifiers like π-bridged 2,4,6-tris(4-aminophenyl)-s-triazine (TAPT), MPS-TMA, and MPA-CPA, increase interfacial surface energy or form chemical bridges, resulting in dense, highly adherent interfaces [95–97]. Bulky aryl-ethyl ammonium cations such as 4-fluoro-phenylethylammonium iodide (F-PEAI) provide dual-side benefits, simultaneously enhancing bottom wetting on poly[bis(4-phenyl)(2,4,6-trimethylphenyl)amine] (PTAA) and passivating the top [6,6]-phenyl-C_{61}-butyric acid methyl ester (PCBM) interface, yielding crack-free films with minimal defect density [98]. Across these categories, common microstructural outcomes, including suppressed voids, reduced groove angles, larger monolithic grains, and relaxed interfacial strain, translate into higher fill factors and remarkable long-term stability (> 90% PCE retention over 1000–1500 h). Beyond surface modifiers, the introduction of advanced interfacial designs, such as chiral-structured heterointerfaces, further demonstrates the potential of microstructure engineering. For instance, incorporating chiral molecules like R-/S-methylbenzyl-ammonium as interlayers between the perovskite and CTL has been shown to enhance both mechanical reliability and chemical stability [44]. The entropy-driven

assembly and tight molecular packing of these chiral structures strengthen the interface and reduce susceptibility to environmental degradation. Modifications to the heterointerface microstructure enable significant improvements in the stability and performance of PSCs, paving the way for their widespread adoption in practical applications.

3 ICD

ICDs represent the microstructural features deeply embedded within perovskite grains. Unlike conventional ceramic materials, perovskites are relatively soft and exhibit a remarkable tolerance for short-range crystalline disorders. These intragrain defects serve a dual purpose: while they are critical in accommodating structural strain and enhancing lattice flexibility, they simultaneously disrupt lattice uniformity. This disruption induces localized strain, which gradually accumulates and ultimately results in performance heterogeneity and long-term instability in PSCs. This section explores the formation and dynamic behavior of ICDs under external stimuli and discusses potential strategies for lattice stabilization through healing mechanisms.

3.1 Atomic-scale imaging of ICDs

The characterization of ICDs at atomic-scale resolution has long been impeded by the sensitivity of MHPs to electron beam damage, which can rapidly degrade sample integrity during transmission electron microscopy (TEM) analysis. To address this, innovative methodologies have been developed, such as the application of protective amorphous carbon coating (~15 nm thick). This method, demonstrated by Cai et al. [41], can stabilize the perovskite structure during prolonged high-resolution scanning TEM (STEM) imaging, preserving its structural and chemical integrity. In addition, TEM observations facilitate the development of accurate computational models based on density functional theory (DFT), improving theoretical descriptions of these ICDs. Such advancements have unveiled diverse ICDs with different dimensions [8,41,99,100], as illustrated in Fig. 6, including one-dimensional (1D) dislocations, 2D stacking faults (SFs), 2D coherent twin boundaries (CTBs), and 3D nanoclusters.

Dislocation defects, as 1D defects shown in Fig. 6(b), can create high-conductivity pathways that enhance charge carrier mobility [101]. However, these lower-dimensional defects primarily affect localized regions within the perovskite lattice, as exemplified by atomic morphologies such as edge dislocations depicted in Fig. 6(f). CTBs represent highly aligned 2D planar defects formed during cubic-to-tetragonal phase transitions, such as those occurring in $MAPbI_3$ during thermal cycling, as shown in Figs. 6(c) and 4(g) [99]. These interfaces span the entire grain thickness and exhibit uniform distribution and reversible formation, which makes them critical for stress mitigation. Owing to their high structural symmetry and minimal lattice distortion, CTBs exert a neutral influence on band alignment and do not introduce deep-level trap states, thus having little effect on charge carrier transport [23]. In mixed halide perovskites, however, the role of CTBs becomes more nuanced. These boundaries can serve as nucleation sites for halide-rich clusters, which, depending on their local bandgap, may act as potential wells or barriers and then introduce subtle modulations in carrier dynamics.

The effects of the above defects are generally less pronounced than those caused by SFs, which are 2D planar defects shown in Fig. 6(d). SFs disrupt the local lattice periodicity and induce significant in-plane strain, often manifesting along both the x and y axes. These defects typically arise during annealing and are highly influenced by processing conditions. Two primary types of SFs have been identified in perovskites: Ruddlesden-Popper SFs (RP-SFs) and partial shift SFs (PS-SFs) [8,33,41,100]. RP-SFs, commonly observed in inorganic perovskites, can propagate extensively within grains, forming characteristic right-angle steps that substantially increase internal strain [100]. Notably, models of RP-SFs in $CsPbBr_3$ reveal minimal disruption to charge transport. The absence of Pb dangling bonds or direct Pb-Pb interactions prevents the formation of deep-level traps, preserving the integrity of the local electronic structure [100]. In contrast, PS-SFs, characteristic of hybrid perovskites, result from minor lattice-plane shifts between adjacent layers. These faults, typically in nanometer length as shown in Fig. 6(d), are localized and introduce significant strain, hampering charge transport and compromising film stability [41]. The impact of SFs also varies across different perovskite compositions. In $FAPbI_3$, SFs primarily align along iodide columns with displacements close to half a unit cell [8], whereas in mixed-cation FA-Cs perovskites, SFs form along lead (Pb^{2+}) columns with a displacement exceeding three-quarters of a unit cell [41]. This variation arises from spatial heterogeneity in FA^+ and Cs^+ incorporation, which induces tensile strain and leads to nanoscale FA-rich clusters. PS-SFs disrupt lattice periodicity, leading to localized strain concentrations manifesting as pronounced lattice distortions within defect regions. These defects increase material brittleness and heighten the risk of strain-induced damage, compromising the structural integrity and stability of the perovskite lattice. DFT calculations demonstrate that SFs increase local bandgap by causing CBM upshifts and VBM downshifts, forming semiconductor-insulator-semiconductor junctions [33]. These regions repel charge carriers, reducing carrier lifetime and decreasing device performance. Furthermore,

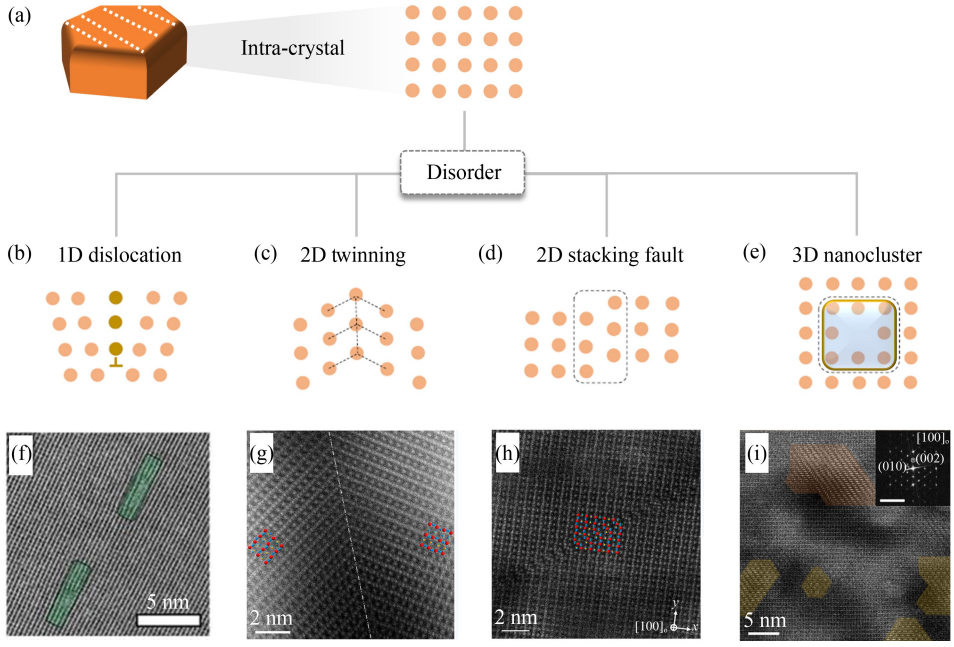

Fig. 6 ICDs of different dimensions. (a) Illustration of ICD within single MHP grains. (b)–(e) Schematic representations of ICD types: (b) 1D dislocation, (c) 2D twinning, (d) 2D SF, and (e) 3D nanoclusters. Reprinted with permission from Ref. [33], copyright 2022, Nature. (f)–(i) Atomic-resolution STEM images of corresponding ICDs: (f) 1D dislocation. Reprinted with permission from Ref. [8], copyright 2020, AAAS. (g) 2D twinning, and (h) 2D SF. Reprinted with permission from Ref. [41], copyright 2022, American Chemical Society. (i) 3D nanoclusters, with labeled regions highlighting defect structures. Reprinted with permission from Ref. [102], copyright 2024, Nature.

the localized effects of PS-SFs are particularly detrimental when their density or distribution is uneven, as they can accumulate to cause localized carrier scattering and significant performance degradation.

In addition to the classic ICD features discussed above, novel microstructures such as nanoclusters have also been identified within perovskite crystals. 3D nanoclusters, primarily present as intragrain impurities (as shown in Fig. 6(e)), form due to suboptimal perovskite film processing conditions, such as insufficient or excessive annealing times. Figure 6(i) illustrates the atomic-scale details of these impurities, with orange and yellow regions representing distinct impurity phases within the film. These intragrain 3D nanocluster impurities generally exhibit limited impact on optoelectronic performance, causing only shallow localized traps near the band edges without introducing deep states in the bandgap [102]. Additionally, at the interface regions, external energy inputs can drive a phase transition from intragrain impurities to perovskite, which will be further discussed in Section 3.2.

The static electronic properties of ICDs are relatively neutral based on theoretical studies, but their dynamic interactions under operational conditions can induce deep trap states with detrimental effects. These 2D and 3D ICDs, while typically benign in isolation, can serve as sinks for highly mobile zero-dimensional (0D) point defects, such as halide vacancies, under external stimuli, as illustrated in Fig. 7. Iodine vacancies in MHPs exhibit high mobility due to their low activation energy. When such vacancies interact with defects like SFs, density of states (DOS) calculations, both total and partial for selected Pb *p* orbitals, show the formation of localized trap states below the conduction band edge (Fig. 7(b)). Similarly, Fig. 7(c) illustrates the charge density near the band edges and the total DOS for PbI_2 nanocluster-perovskite interfaces along the perovskite $(01\bar{1})$ and (011) planes, with one iodine interstitial per supercell. The localized trap states introduced at the interface are primarily associated with the *p* orbitals of Pb and I atoms near the defects. These observations underscore a critical insight: while ICDs may not impede charge transport, their interactions with mobile point defects can degrade the electronic structure and introduce deep trap states, ultimately reducing device performance over time [41,102].

The dual nature of ICDs, being either neutral or detrimental, depends heavily on their interactions with other defects and external stimuli, making it imperative to understand and control their formation and behavior. To suppress the emergence of high-energy ICDs, controlling the crystallization process is essential. Techniques such as solvent engineering and temperature modulation can promote uniform crystal growth, minimizing the occurrence of structural irregularities. Additionally, incorporating passivating agents or dopants offers an effective strategy to reduce defect migration by increasing activation energy barriers, thus mitigating harmful

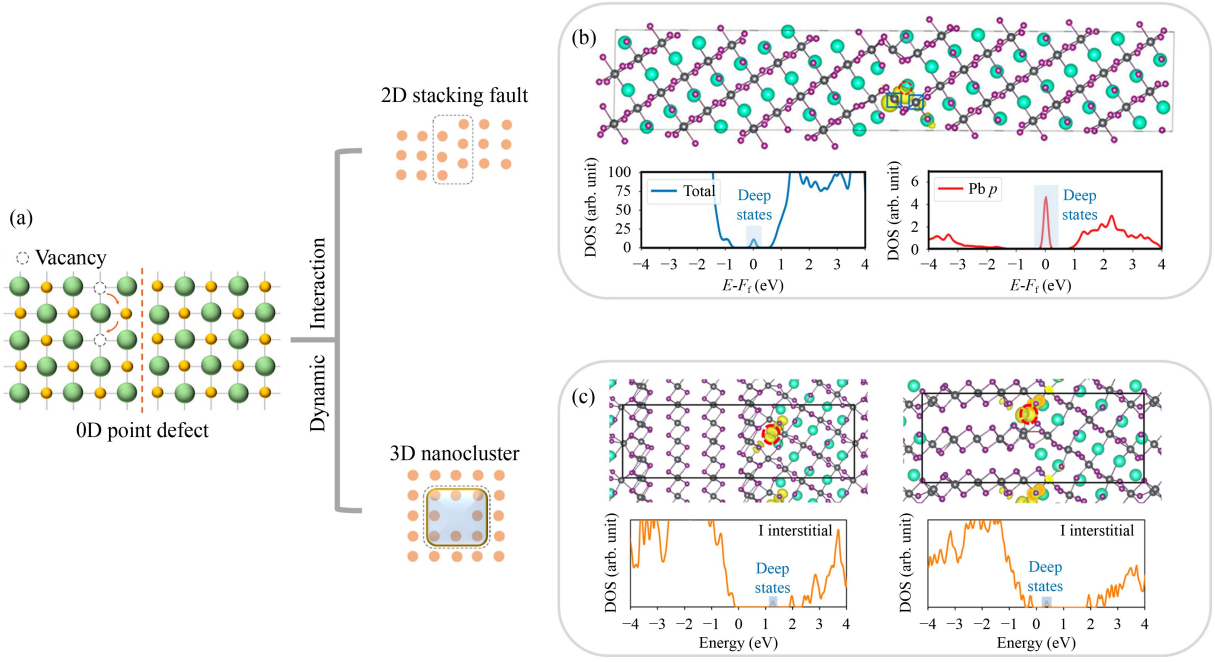

Fig. 7 Dynamic interaction of ICDs with migrating 0D point defects. (a) Schematic illustration of interactions involving I^- vacancies. Reprinted with permission from Ref. [41], copyright 2022, American Chemical Society. (b) The charge density of trap states below the Fermi level, along with total and partial DOS of selected Pb *p* orbitals at the 2D stacking-fault interface. Reprinted with permission from Ref. [41], copyright 2022, American Chemical Society. (c) Charge density near the band edges and total DOS for PbI_2 nanocluster-perovskite interfaces along perovskite (01$\bar{1}$) (left panel) and (011) (right panel) plane with one I interstitials (per supercell) (in (b, c), cyan, black, and purple spheres represent FA/Cs, Pb, and I atoms, respectively, and the yellow regions depict the calculated charge density. The red dashed circle marks the I interstitial, and blue squares indicate the selected Pb atoms). Reprinted with permission from Ref. [102], copyright 2024, Nature.

interactions between ICDs and mobile point defects like halide vacancies. A deeper investigation of the dynamic behavior and stability mechanisms of yet-undiscovered ICDs under operational conditions is urgently needed. Such breakthroughs require advanced *in situ* characterization techniques capable of capturing the formation, evolution, and interactions of ICDs during device operation.

3.2 *In situ* dynamics of ICDs

Unraveling the stability mechanisms of perovskite devices under operational conditions demands advancements in *in situ* characterization techniques that enable direct visualization of dynamic processes under realistic environments. Light plays a dual role in perovskite materials. While it activates exceptional functionalities of MHPs, it can also induce material transformations and degradation, thereby impacting device performance and long-term stability. In particular, the dynamic behavior of ICDs has been proven to be influenced by external light stimuli, making their responses under operational conditions a key focus for unraveling the stability and performance of PSCs. A major technical challenge lies in adapting commercial *in situ* TEM platforms to integrate reliable light sources and facilitate multi-factor parallel control, including the simultaneous manipulation of light, temperature, and electric fields.

Advanced methodologies, such as on-chip light-incorporated *in situ* TEM (LI^2ST) [103], have been developed to bridge fundamental defect studies with practical device optimization. This technique integrates micro-LEDs into TEM holders, enabling simultaneous observation of nanoscale structural dynamics, phase transitions, and optoelectronic property changes under controlled illumination. The LI^2ST platform design, illustrated in Fig. 8(a), facilitates real-time tracking of the dynamic behavior of perovskite grains. Time-resolved TEM imaging and selected area electron diffraction (SAED) patterns (Figs. 8(b)–8(i)) reveal how light exposure triggers phase transitions and crystallographic changes over time. When $CsPbBr_3$ grains are illuminated, additional diffraction spots emerge in patterns from the same region, indicating the formation of new phases potentially associated with $PbBr_2$. Subsequent *ex-situ* high-resolution STEM observations provided structural insights into these transformations, confirming that light-induced degradation in polycrystalline perovskites predominantly originates within grains. This challenges the traditional assumption that degradation starts in GBs. Under continuous illumination, Br^- and photogenerated holes (h^+) undergo reactions, showing the presence of ion conduction. Interestingly, GBs, which often exhibit non-radiative recombination and shorter carrier lifetimes for

photogenerated electron-hole pairs, are less likely to drive Br^- and h^+ reactions. This degradation localized within grains remains confined to specific regions, in contrast to GB-driven degradation, which propagates extensively through interconnected 3D networks.

Notably, ICDs in PSCs exhibit self-healing properties under controlled stimuli, such as low-dose lasers and electron beams, demonstrating the intrinsic resilience and defect-tolerant nature of perovskites. Perovskite lattices are intrinsically vulnerable to high-energy stimuli, so electron-beam protocol intended to heal ICDs needs to balance the defect-activation threshold against the damage threshold of pristine domains. Probe current of ≈ 1 pA is sufficient to trigger intragrain impurity annihilation and phase healing, whereas increasing the dose to ≈ 10 pA collapses the lattice through halide loss and framework rupture [102]. Analogously, ultrafast laser annealing of perovskite films can be tuned to operate below the photo-decomposition threshold [104]. Collectively, the cumulative energy dose is the decisive parameter: by operating in a low-dose/low-fluence regime and lengthening the exposure time, one can drive ion-redistribution-mediated self-repair and avoid collateral degradation of defect-free lattice areas. For example, Fig. 8(j) illustrates the experimental setup for *in situ* STEM characterization, where the electron beam serves not only as a structural probe but also as a stimulus to induce crystallographic transitions. Atomic-resolution STEM-HAADF imaging of orthorhombic (FA, Cs) PbI_3, shown in Fig. 6(i), reveals PbI_2 3D nanoclusters (marked by orange dashed lines) embedded in the perovskite lattice. Under continuous electron beam scanning, this nanocluster transforms into a perovskite phase through atomic-scale phase healing, as shown in Fig. 8(k). This transformation demonstrates ICD's ability to restore lattice uniformity and mitigate strain through self-healing mechanisms. The corresponding out-of-plane strain distribution, shown in Fig. 8(l), further illustrates how this transformation relaxes intragrain strain caused by impurity. This healing process is driven by the redistribution of ions and vacancies under thermodynamic forces, which seek to minimize the system's free energy. The propagation of reaction fronts through defective regions restores lattice continuity, substantially reducing both trap density and local strain energy. DFT analyses corroborate these findings, indicating that phase healing

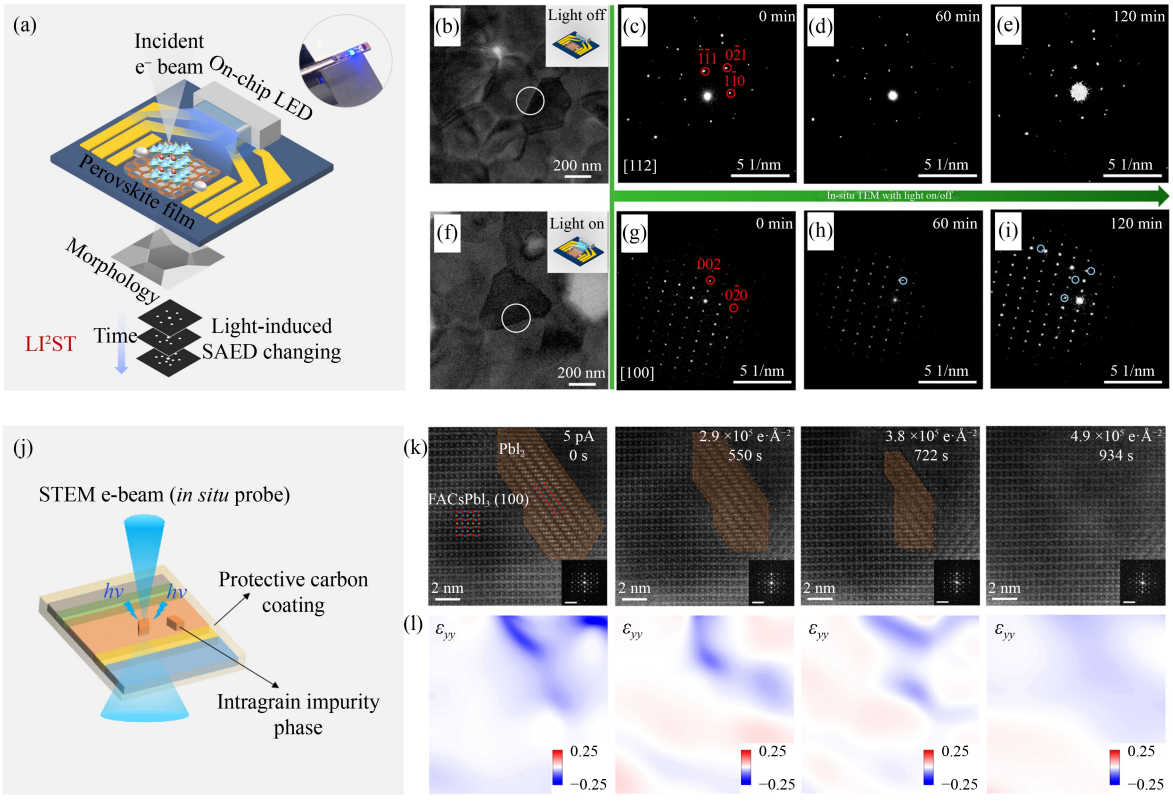

Fig. 8 *In situ* TEM observation of ICDs dynamics. (a) Schematic of the on-chip LI^{2}ST method for visualizing light-triggered dynamics of perovskite grain. (b) and (f) TEM images, (c)–(e) and (g)–(i) SAED patterns showing time-dependent changes (0, 60, 120 min) in perovskite crystallographic phases under light-off and light-on conditions. (a)–(i) Reprinted with permission from Ref. [103], copyright 2023, American Chemical Society. (j) Schematic of *in situ* STEM observation showing the use of the electron beam for structural characterization and stimulation of phase transformation; (k) atomic-resolution STEM-HAADF (high-angle annular dark field) images showing the transformation of PbI_2 nanocluster to the perovskite phase under continuous electron probe scanning, with FFT patterns as insets (scale bar: 4 nm^{-1}); (l) out-of-plane strain (ε_{yy}) distributions analyzed by GPA, showing strain relaxation due to impurity annihilation. Reprinted with permission from Ref. [102], copyright 2024, Nature.

reduces electronic trap states and local energy barriers. These transformations enhance charge carrier mobility and extend carrier lifetimes, directly improving device performance. Inspired by these insights, innovative strategies have been developed to translate atomic-level fundamental findings into module-level device technologies. For instance, laser-induced intragrain impurity annihilation has been employed to selectively target defective regions within grains, thereby enhancing structural uniformity [102].

Current advancements in *in situ* techniques, such as those incorporating light, temperature, and environmental factors like humidity and oxygen, enable real-time observation of defect evolution and phase transitions within perovskite materials. These methods provide valuable insights into how light and thermal effects drive degradation processes, such as strain accumulation and halide-ion migration, particularly within grains. Future studies expanding these *in situ* platforms to include a broader range of environmental variables will enhance our understanding of defect interactions and self-healing mechanisms, guiding the design of more robust, high-performance perovskite materials. By integrating advanced characterization techniques with defect engineering strategies, researchers can systematically address degradation challenges, improving carrier mobility, lifetime, and overall device stability.

4 Conclusions and outlook

The transition from microstructure observation to microstructure control marks the next frontier in perovskite photovoltaics. The past decade has witnessed remarkable progress in exploring microstructural disorders in MHPs, with seminal studies elucidating their origins, dynamic evolution, and correlations with device performance and long-term stability. Particularly, the photo-mechanical properties of PSCs under operational stresses have emerged as a critical determinant of stability, where crack propagation often initiates at microstructural disorders. The paradigm shift from passive defect suppression to active microstructure engineering requires a holistic strategy, akin to assembling a complex puzzle, that integrates advanced experimental characterization, theoretical modeling, and artificial intelligence (AI)-driven engineering, ensuring their effective synergy.

The priority is to develop high-performance characterization techniques capable of uncovering the dynamic behaviors and hidden microstructure anomalies that cumulatively affect the photochemical processes and mechanical properties of PSCs. Recent advancements in characterization techniques, particularly *in situ* TEM [41,102] and LI^{2}ST platform [103], offer opportunities to observe the dynamic evolution of microstructure defects. Further development is needed in multi-modal real-time monitoring approaches that combine light, electrical, and thermal dynamic characterization techniques. These approaches can reveal dynamic behaviors of the complex structural changes that materials experience under operational conditions. Experimental observations of microstructural features provide a foundation for integrating theoretical modeling to enhance defect management strategies. DFT-based multi-scale simulations can mimic the distribution and interactions of microstructural defects within crystal grains [41,102]. These simulations provide critical mechanisms into how defects influence electronic transport, guiding defect engineering, interface modification, and additive selection.

A longstanding bottleneck in perovskite research and materials science more broadly lies in quantifying the structure-property relationship. Traditional paradigms often rely on qualitative microstructural descriptions, making it challenging to establish precise, formulaic correlations with quantitative property metrics. Therefore, the first step is to move beyond traditional localized grain analysis and focus on quantifying microstructural characteristics across entire thin films. The advent of *in situ* and real-time characterization techniques has exponentially increased the volume and complexity of high-dimensional data, necessitating advanced tools for interpretation. Data-driven methods, such as machine vision algorithms, particularly convolutional neural networks, have demonstrated exceptional capabilities in automating microstructure analysis. Applied to scanning electron microscopy and AFM images, these methods enable efficient quantification of key parameters like average grain surface area, GB geometries, and intragrain surface fluctuations with minimal manual intervention [105–107]. AI-powered statistical analyses of large-scale microstructure datasets demonstrate the potential to identify specific defect types, quantify their impacts, and parameterize features with precision. By uncovering trends and correlations within grain property distributions across entire films, these methods reveal insights that would otherwise remain hidden, enabling researchers to transition from isolated observations to systematic investigation. The next crucial step involves establishing precise and reliable correlations between parameterized microstructure characteristics and macroscopic device performance metrics.

Achieving effective microstructure control lies in reconciling thermodynamic stability, a multidimensional issue governed by complex phase transitions and crystallization kinetics within MHPs. Buried interface engineering emerges as a critical leverage point, as the nucleation behavior at substrate/perovskite interfaces dictates both the crystallographic orientation of subsequent film growth and the spatial distribution of GB [108,109]. Building on this foundation, synergistic

strategies combining additive engineering for precursor solution coordination with gradient annealing enable dual control over grain size distribution and boundary characteristics [20]. However, this multi-parameter optimization introduces a high-dimensional processing parameter space. The integration of high-throughput experimentation with machine learning-driven correlation analysis offers a pathway to decode hidden relationships between processing parameters and microstructural evolution. Transforming conventional defect passivation strategies into a predictive microstructure design approach, guided by strain field regulation and interface reconstruction, will be key to unlocking the full potential of PSCs, accelerating both scalable manufacturing and long-term operational stability.

Competing interests The authors declare that they have no competing interests.

Acknowledgements Zhou Y acknowledges the Excellent Young Scientists Fund (Grant No. 52222318) from the National Natural Science Foundation of China, the General Research Fund (Grant Nos. 12302822 and 12300923) and the Collaborative Research Fund (Grant No. C2001-23Y) from the Hong Kong Research Grants Council of China (RGC), the NSFC/RGC Collaborative Research Scheme of China (Grant No. CRS-HKUST203/23), and the startup grant from the HKUST.

Funding Note: Open access funding provided by Hong Kong University of Science and Technology.

References

1. NREL BestResearch-Cell Efficiency Chart. 2005
2. Kojima A, Teshima K, Shirai Y, Miyasaka T. Organometal halide perovskites as visible-light sensitizers for photovoltaic cells. Journal of the American Chemical Society, 2009, 131(17): 6050–6051
3. Brandt R E, Poindexter J R, Gorai P, Kurchin R C, Hoye R L Z, Nienhaus L, Wilson M W B, Polizzotti J A, Sereika R, Žaltauskas R, et al. Searching for "defect-tolerant" photovoltaic materials: combined theoretical and experimental screening. Chemistry of Materials, 2017, 29(11): 4667–4674
4. Brandt R E, Stevanović V, Ginley D S, Buonassisi T. Identifying defect-tolerant semiconductors with high minority-carrier lifetimes: beyond hybrid lead halide perovskites. MRS Communications, 2015, 5(2): 265–275
5. Brenner T M, Egger D A, Kronik L, Hodes G, Cahen D. Hybrid organic-inorganic perovskites: low-cost semiconductors with intriguing charge-transport properties. Nature Reviews: Materials, 2016, 1(1): 15007
6. Ball J M, Petrozza A. Defects in perovskite-halides and their effects in solar cells. Nature Energy, 2016, 1(11): 16149
7. Zhou Y, Game O S, Pang S, Padture N P. Microstructures of organometal trihalide perovskites for solar cells: their evolution from solutions and characterization. Journal of Physical Chemistry Letters, 2015, 6(23): 4827–4839
8. Rothmann M U, Kim J S, Borchert J, Lohmann K B, O'Leary C M, Sheader A A, Clark L, Snaith H J, Johnston M B, Nellist P D, et al. Atomic-scale microstructure of metal halide perovskite. Science, 2020, 370(6516): eabb5940
9. Dunlap-Shohl W A, Zhou Y, Padture N P, Mitzi D B. Synthetic approaches for halide perovskite thin films. Chemical Reviews, 2019, 119(5): 3193–3295
10. Li W, Yadavalli S K, Lizarazo-Ferro D, Chen M, Zhou Y, Padture N P, Zia R. Subgrain special boundaries in halide perovskite thin films restrict carrier diffusion. ACS Energy Letters, 2018, 3(11): 2669–2670
11. Yun J S, Kim J, Young T, Patterson R J, Kim D, Seidel J, Lim S, Green M A, Huang S, Ho-Baillie A. Humidity-induced degradation via grain boundaries of $HC(NH_2)_2PbI_3$ planar perovskite solar cells. Advanced Functional Materials, 2018, 28(11): 1705363
12. Zong Y, Zhou Y, Zhang Y, Li Z, Zhang L, Ju M G, Chen M, Pang S, Zeng X C, Padture N P. Continuous grain-boundary functionalization for high-efficiency perovskite solar cells with exceptional stability. Chem, 2018, 4(6): 1404–1415
13. Zong Y, Zhou Z, Chen M, Padture N P, Zhou Y. Lewis-adduct mediated grain-boundary functionalization for efficient ideal-bandgap perovskite solar cells with superior stability. Advanced Energy Materials, 2018, 8(27): 1800997
14. Tang X, van den Berg M, Gu E, Horneber A, Matt G J, Osvet A, Meixner A J, Zhang D, Brabec C J. Local observation of phase segregation in mixed-halide perovskite. Nano Letters, 2018, 18(3): 2172–2178
15. Meggiolaro D, Mosconi E, De Angelis F. Formation of surface defects dominates ion migration in lead-halide perovskites. ACS Energy Letters, 2019, 4(3): 779–785
16. Stecker C, Liu K, Hieulle J, Ohmann R, Liu Z, Ono L K, Wang G, Qi Y. Surface defect dynamics in organic-inorganic hybrid perovskites: from mechanism to interfacial properties. ACS Nano, 2019, 13(10): 12127–12136
17. Li F, Deng X, Qi F, Li Z, Liu D, Shen D, Qin M, Wu S, Lin F, Jang S H, et al. Regulating surface termination for efficient inverted perovskite solar cells with greater than 23% efficiency. Journal of the American Chemical Society, 2020, 142(47): 20134–20142
18. Zheng G, Zhu C, Ma J, Zhang X, Tang G, Li R, Chen Y, Li L, Hu J, Hong J, et al. Manipulation of facet orientation in hybrid perovskite polycrystalline films by cation cascade. Nature Communications, 2018, 9(1): 2793
19. Leblebici S Y, Leppert L, Li Y, Reyes-Lillo S E, Wickenburg S, Wong E, Lee J, Melli M, Ziegler D, Angell D K, et al. Facet-

dependent photovoltaic efficiency variations in single grains of hybrid halide perovskite. Nature Energy, 2016, 1(8): 16093

20. Hao M, Zhou Y. Grain-boundary grooves in perovskite solar cells. Joule, 2024, 8(4): 913–921
21. Hao M, Duan T, Ma Z, Ju M G, Bennett J A, Liu T, Guo P, Zhou Y. Flattening grain-boundary grooves for perovskite solar cells with high optomechanical reliability. Advanced Materials, 2023, 35: 2211155
22. Xiao T, Hao M, Duan T, Li Y, Zhang Y, Guo P, Zhou Y. Elimination of grain surface concavities for improved perovskite thin-film interfaces. Nature Energy, 2024, 9(8): 999
23. Xiao X, Li W, Fang Y, Liu Y, Shao Y, Yang S, Zhao J, Dai X, Zia R, Huang J. Benign ferroelastic twin boundaries in halide perovskites for charge carrier transport and recombination. Nature Communications, 2020, 11(1): 2215
24. Jiang J, Sun X, Chen X, Wang B, Chen Z, Hu Y, Guo Y, Zhang L, Ma Y, Gao L, et al. Carrier lifetime enhancement in halide perovskite via remote epitaxy. Nature Communications, 2019, 10(1): 4145
25. Yao W, Fang S, Hu Z, Huang L, Liu X, Zhang H, Zhang J, Zhu Y. Dependence of the heterogeneity of grain boundaries on adjacent grains in perovskites and its impact on photovoltage. Small, 2022, 18(8): 2105140
26. Qin T X, You E M, Zhang M X, Zheng P, Huang X F, Ding S Y, Mao B W, Tian Z Q. Quantification of electron accumulation at grain boundaries in perovskite polycrystalline films by correlative infrared-spectroscopic nanoimaging and Kelvin probe force microscopy. Light, Science & Applications, 2021, 10(1): 84
27. Adhyaksa G W P, Brittman S, Abolins H, Lof A, Li X, Keelor J D, Luo Y, Duevski T, Heeren R M A, Ellis S R, et al. Understanding detrimental and beneficial grain boundary effects in halide perovskites. Advanced Materials, 2018, 30(52): 1804792
28. Edri E, Kirmayer S, Henning A, Mukhopadhyay S, Gartsman K, Rosenwaks Y, Hodes G, Cahen D. Why lead methylammonium tri-iodide perovskite-based solar cells require a mesoporous electron transporting scaffold (but not necessarily a hole conductor). Nano Letters, 2014, 14(2): 1000–1004
29. Long R, Prezhdo O V. Instantaneous generation of charge-separated state on TiO_2 surface sensitized with plasmonic nanoparticles. Journal of the American Chemical Society, 2014, 136(11): 4343–4354
30. Yun J S, Ho-Baillie A, Huang S, Woo S H, Heo Y, Seidel J, Huang F, Cheng Y B, Green M A. Benefit of grain boundaries in organic-inorganic halide planar perovskite solar cells. Journal of Physical Chemistry Letters, 2015, 6(5): 875–880
31. Kim G Y, Oh S H, Nguyen B P, Jo W, Kim B J, Lee D G, Jung H S. Efficient carrier separation and intriguing switching of bound charges in inorganic-organic lead halide solar cells. Journal of Physical Chemistry Letters, 2015, 6(12): 2355–2362
32. Yin W J, Shi T, Yan Y. Unique properties of halide perovskites as possible origins of the superior solar cell performance. Advanced Materials, 2014, 26(27): 4653–4658
33. Zhou Y, Herz L M, Jen A K Y, Saliba M. Advances and challenges in understanding the microscopic structure-property-performance relationship in perovskite solar cells. Nature Energy, 2022, 7(9): 794–807
34. Eames C, Frost J M, Barnes P R F, O'Regan B C, Walsh A, Islam M S. Ionic transport in hybrid lead iodide perovskite solar cells. Nature Communications, 2015, 6(1): 7497
35. Haruyama J, Sodeyama K, Han L, Tateyama Y. First-principles study of ion diffusion in perovskite solar cell sensitizers. Journal of the American Chemical Society, 2015, 137(32): 10048–10051
36. Yuan Y, Huang J. Ion migration in organometal trihalide perovskite and its impact on photovoltaic efficiency and stability. Accounts of Chemical Research, 2016, 49(2): 286–293
37. Li J, Dong Q, Li N, Wang L. Direct evidence of ion diffusion for the silver-electrode-induced thermal degradation of inverted perovskite solar cells. Advanced Energy Materials, 2017, 7(14): 1602922
38. Kato Y, Ono L K, Lee M V, Wang S, Raga S R, Qi Y. Silver iodide formation in methyl ammonium lead iodide perovskite solar cells with silver top electrodes. Advanced Materials Interfaces, 2015, 2(13): 1500195
39. Domanski K, Correa-Baena J P, Mine N, Nazeeruddin M K, Abate A, Saliba M, Tress W, Hagfeldt A, Grätzel M. Not all that glitters is gold: metal-migration-induced degradation in perovskite solar cells. ACS Nano, 2016, 10(6): 6306–6314
40. Li Y, Xu X, Wang C, Ecker B, Yang J, Huang J, Gao Y. Light-induced degradation of $CH_3NH_3PbI_3$ hybrid perovskite thin film. Journal of Physical Chemistry C, 2017, 121(7): 3904–3910
41. Cai S, Dai J, Shao Z, Rothmann M U, Jia Y, Gao C, Hao M, Pang S, Wang P, Lau S P, et al. Atomically resolved electrically active intragrain interfaces in perovskite semiconductors. Journal of the American Chemical Society, 2022, 144(4): 1910–1920
42. Chen P, Xiao Y, Hu J, Li S, Luo D, Su R, Caprioglio P, Kaienburg P, Jia X, Chen N, et al. Multifunctional ytterbium oxide buffer for perovskite solar cells. Nature, 2024, 625(7995): 516–522
43. Dai Z, Yadavalli S K, Chen M, Abbaspourtamijani A, Qi Y, Padture N P. Interfacial toughening with self-assembled monolayers enhances perovskite solar cell reliability. Science, 2021, 372(6542): 618–622
44. Duan T, You S, Chen M, Yu W, Li Y, Guo P, Berry J J, Luther J M, Zhu K, Zhou Y. Chiral-structured heterointerfaces enable durable perovskite solar cells. Science, 2024, 384(6698): 878–884
45. Lee J W, Tan S, Seok S I, Yang Y, Park N G. Rethinking the A cation in halide perovskites. Science, 2022, 375(6583): eabj1186
46. Jung E H, Jeon N J, Park E Y, Moon C S, Shin T J, Yang T Y, Noh J H, Seo J. Efficient, stable, and scalable perovskite solar cells using poly(3-hexylthiophene). Nature, 2019, 567(7749): 511–515
47. Jiang Q, Zhao Y, Zhang X, Yang X, Chen Y, Chu Z, Ye Q, Li X, Yin Z, You J. Surface passivation of perovskite film for efficient solar cells. Nature Photonics, 2019, 13(7): 460–466
48. Yoo J J, Wieghold S, Sponseller M C, Chua M R, Bertram S N, Hartono N T P, Tresback J S, Hansen E C, Correa-Baena J P, Bulovic V, et al. An interface stabilized perovskite solar cell with high stabilized efficiency and low voltage loss. Energy &

Environmental Science, 2019, 12(7): 2192–2199
49. Yang Y, Xiong Q, Wu J, Tu Y, Sun T, Li G, Liu X, Wang X, Du Y, Deng C, et al. Poly(3-hexylthiophene)/perovskite heterointerface by spinodal decomposition enabling efficient and stable perovskite solar cells. Advanced Materials, 2024, 36(7): 2310800
50. Wang S, Sakurai T, Wen W, Qi Y. Energy level alignment at interfaces in metal halide perovskite solar cells. Advanced Materials Interfaces, 2018, 5(22): 1800260
51. Sakhatskyi K, John R A, Guerrero A, Tsarev S, Sabisch S, Das T, Matt G J, Yakunin S, Cherniukh I, Kotyrba M, et al. Assessing the drawbacks and benefits of ion migration in lead halide perovskites. ACS Energy Letters, 2022, 7(10): 3401–3414
52. Chen J, Wang X, Wang T, Li J, Chia H Y, Liang H, Xi S, Liu S, Guo X, Guo R, et al. Determining the bonding-degradation trade-off at heterointerfaces for increased efficiency and stability of perovskite solar cells. Nature Energy, 2025, 10: 181–190
53. De Bastiani M, Armaroli G, Jalmood R, Ferlauto L, Li X, Tao R, Harrison G T, Eswaran M K, Azmi R, Babics M, et al. Mechanical reliability of fullerene/tin oxide interfaces in monolithic perovskite/silicon tandem cells. ACS Energy Letters, 2022, 7(2): 827–833
54. Zhang H, Pfeifer L, Zakeeruddin S M, Chu J, Grätzel M. Tailoring passivators for highly efficient and stable perovskite solar cells. Nature Reviews Chemistry, 2023, 7(9): 632–652
55. Yusoff A. R bin M, Vasilopoulou M, Georgiadou D G, Palilis L C, Abate A, Nazeeruddin M K. Passivation and process engineering approaches of halide perovskite films for high efficiency and stability perovskite solar cells. Energy & Environmental Science, 2021, 14(5): 2906–2953
56. Cai W, Wang Y, Shang W, Liu J, Wang M, Dong Q, Han Y, Li W, Ma H, Wang P, et al. Lewis base governing superfacial proton behavior of hybrid perovskite: basicity dependent passivation strategy. Chemical Engineering Journal, 2022, 446: 137033
57. Cao Q, Wang T, Yang J, Zhang Y, Li Y, Pu X, Zhao J, Chen H, Li X, Tojiboyev I, et al. Environmental-friendly polymer for efficient and stable inverted perovskite solar cells with mitigating lead leakage. Advanced Functional Materials, 2022, 32(32): 2201036
58. Ni Z, Bao C, Liu Y, Jiang Q, Wu W Q, Chen S, Dai X, Chen B, Hartweg B, Yu Z, et al. Resolving spatial and energetic distributions of trap states in metal halide perovskite solar cells. Science, 2020, 367(6484): 1352–1358
59. Wei K, Yang L, Deng J, Luo Z, Zhang X, Zhang J. Facile exfoliation of the perovskite thin film for visualizing the buried interfaces in perovskite solar cells. ACS Applied Energy Materials, 2022, 5(6): 7458–7465
60. Mohamad Noh M F, Arzaee N A, Harif M N, Mat Teridi M A, Mohd Yusoff A, Mahmood Zuhdi A W. Defect engineering at buried interface of perovskite solar cells. Small Methods, 2024, 8(12): 2400385
61. Nukunudompanich M, Suzuki K, Kameda K, Manzhos S, Ihara M. Nano-scale smooth surface of the compact-TiO_2 layer via spray pyrolysis for controlling the grain size of the perovskite layer in perovskite solar cells. RSC Advances, 2023, 13(40): 27686–27695
62. Zhao L, Tang P, Luo D, Dar M I, Eickemeyer F T, Arora N, Hu Q, Luo J, Liu Y, Zakeeruddin S M, et al. Enabling full-scale grain boundary mitigation in polycrystalline perovskite solids. Science Advances, 2022, 8(35): eabo3733
63. Akyildiz O, Ogurtani T O. Thermal grooving by surface diffusion: a review of classical thermo-kinetics approach. Hittite Journal of Science and Engineering, 2017, 4(1): 7–16
64. Mullins W W. Theory of thermal grooving. Journal of Applied Physics, 1957, 28(3): 333–339
65. Wang M, Fei C, Uddin M A, Huang J. Influence of voids on the thermal and light stability of perovskite solar cells. Science Advances, 2022, 8(38): eabo5977
66. Shao Y, Fang Y, Li T, Wang Q, Dong Q, Deng Y, Yuan Y, Wei H, Wang M, Gruverman A, et al. Grain boundary dominated ion migration in polycrystalline organic-inorganic halide perovskite films. Energy & Environmental Science, 2016, 9(5): 1752–1759
67. Xue D J, Hou Y, Liu S C, Wei M, Chen B, Huang Z, Li Z, Sun B, Proppe A H, Dong Y, et al. Regulating strain in perovskite thin films through charge-transport layers. Nature Communications, 2020, 11(1): 1514
68. Jacobsson T J, Schwan L J, Ottosson M, Hagfeldt A, Edvinsson T. Determination of thermal expansion coefficients and locating the temperature-induced phase transition in methylammonium lead perovskites using X-ray diffraction. Inorganic Chemistry, 2015, 54(22): 10678–10685
69. Hackl K, Fischer F D, Svoboda J. A variational approach to the modelling of grooving in a three-dimensional setting. Acta Materialia, 2017, 129: 331–342
70. Zhao B, Shvindlerman L, Gottstein G. On the orientation dependence of grain boundary triple line energy in Cu. International Journal of Materials Research, 2014, 105(12): 1151–1158
71. Liang Z, Zhang Y, Xu H, Chen W, Liu B, Zhang J, Zhang H, Wang Z, Kang D H, Zeng J, et al. Homogenizing out-of-plane cation composition in perovskite solar cells. Nature, 2023, 624(7992): 557–563
72. Bai Y, Huang Z, Zhang X, Lu J, Niu X, He Z, Zhu C, Xiao M, Song Q, Wei X, et al. Initializing film homogeneity to retard phase segregation for stable perovskite solar cells. Science, 2022, 378(6621): 747–754
73. Hao M, Yang J, Yu W, Lawrie B J, Guo P, Zhang X, Duan T, Xiao T, Chen L, Xiang Y, et al. Nanoscopic cross-grain cation homogenization in perovskite solar cells. Nature Nanotechnology, 2025, 20(5): 630
74. Zhao B, Shvindlerman L, Gottstein G. Line tension of grain boundary triple junctions in the copper tricrystals. In: TMS 2014 143rd Annual Meeting & Exhibition. Cham: Springer, 2014, 1063–1068
75. Saylor D M, Rohrer G S. Measuring the influence of grain-boundary misorientation on thermal groove geometry in ceramic polycrystals. Journal of the American Ceramic Society, 1999, 82(6): 1529–1536
76. Mullins W W. The effect of thermal grooving on grain boundary motion. Acta Metallurgica, 1958, 6(6): 414–427

77. Saidaminov M I, Williams K, Wei M, Johnston A, Quintero-Bermudez R, Vafaie M, Pina J M, Proppe A H, Hou Y, Walters G, et al. Multi-cation perovskites prevent carrier reflection from grain surfaces. Nature Materials, 2020, 19(4): 412–418
78. Jiang J, Shi M, Xia Z, Cheng Y, Chu Z, Zhang W, Li J, Yin Z, You J, Zhang X. Efficient pure-red perovskite light-emitting diodes with strong passivation via ultrasmall-sized molecules. Science Advances, 2024, 10(18): eadn5683
79. Li T, Wang S, Yang J, Pu X, Gao B, He Z, Cao Q, Han J, Li X. Multiple functional groups synergistically improve the performance of inverted planar perovskite solar cells. Nano Energy, 2021, 82: 105742
80. Jeong J, Kim M, Seo J, Lu H, Ahlawat P, Mishra A, Yang Y, Hope M A, Eickemeyer F T, Kim M, et al. Pseudo-halide anion engineering for α-$FAPbI_3$ perovskite solar cells. Nature, 2021, 592(7854): 381–385
81. Tao S, Schmidt I, Brocks G, Jiang J, Tranca I, Meerholz K, Olthof S. Absolute energy level positions in tin- and lead-based halide perovskites. Nature Communications, 2019, 10(1): 2560
82. Chen Y, Yang N, Zheng G, Pei F, Zhou W, Zhang Y, Li L, Huang Z, Liu G, Yin R, et al. Nuclei engineering for even halide distribution in stable perovskite/silicon tandem solar cells. Science, 2024, 385(6708): 554–560
83. Zhou Z, Liang J, Zhang Z, Zheng Y, Wu X, Tian C, Huang Y, Wang J, Yang Y, Sun A, et al. Direct *in situ* conversion of lead iodide to a highly oriented and crystallized perovskite thin film via sequential deposition for 23.48% efficient and stable photovoltaic devices. ACS Applied Materials & Interfaces, 2022, 14(44): 49886–49897
84. Dai J, Xiong J, Liu N, He Z, Zhang Y, Zhan S, Fan B, Liu W, Huang X, Hu X, et al. Synergistic dual-interface modification strategy for highly reproducible and efficient PTAA-based inverted perovskite solar cells. Chemical Engineering Journal, 2023, 453: 139988
85. Luo C, Zheng G, Gao F, Wang X, Zhan C, Gao X, Zhao Q. Engineering the buried interface in perovskite solar cells via lattice-matched electron transport layer. Nature Photonics, 2023, 17(10): 856–864
86. Hu H, Ritzer D B, Diercks A, Li Y, Singh R, Fassl P, Jin Q, Schackmar F, Paetzold U W, Nejand B A. Void-free buried interface for scalable processing of *p-i-n*-based $FAPbI_3$ perovskite solar modules. Joule, 2023, 7(7): 1574–1592
87. Fei C, Li N, Wang M, Wang X, Gu H, Chen B, Zhang Z, Ni Z, Jiao H, Xu W, et al. Lead-chelating hole-transport layers for efficient and stable perovskite minimodules. Science, 2023, 380(6647): 823–829
88. Chen S, Xiao X, Chen B, Kelly L L, Zhao J, Lin Y, Toney M F, Huang J. Crystallization in one-step solution deposition of perovskite films: upward or downward? Science Advances, 2021, 7(4): eabb2412
89. Chen S, Dai X, Xu S, Jiao H, Zhao L, Huang J. Stabilizing perovskite-substrate interfaces for high-performance perovskite modules. Science, 2021, 373(6557): 902–907
90. Nix W D, Clemens B M. Crystallite coalescence: a mechanism for intrinsic tensile stresses in thin films. Journal of Materials Research, 1999, 14(8): 3467–3473
91. Zou Y, Guo R, Buyruk A, Chen W, Xiao T, Yin S, Jiang X, Kreuzer L P, Mu C, Ameri T, et al. Sodium dodecylbenzene sulfonate interface modification of methylammonium lead iodide for surface passivation of perovskite solar cells. ACS Applied Materials & Interfaces, 2020, 12(47): 52643–52651
92. Wang T, Xie M, Abbasi S, Cheng Z, Liu H, Shen W. High efficiency perovskite solar cells with tailorable surface wettability by surfactant. Journal of Power Sources, 2020, 448: 227584
93. Yuan S, Zheng D, Zhang T, Wang Y, Qian F, Wang L, Li X, Zheng H, Diao Z, Zhang P, et al. Scalable preparation of perovskite films with homogeneous structure via immobilizing strategy for high-performance solar modules. Nature Communications, 2025, 16(1): 2052
94. Sun J, Chen W, Ren Y, Niu Y, Yang Z, Mo L, Huang Y, Li Z, Zhang H, Hu L. Molecular exchange and passivation at interface afford high-performing perovskite solar cells with efficiency over 24%. Journal of Energy Chemistry, 2023, 82: 219–227
95. Zhang S, Ye F, Wang X, Chen R, Zhang H, Zhan L, Jiang X, Li Y, Ji X, Liu S, et al. Minimizing buried interfacial defects for efficient inverted perovskite solar cells. Science, 2023, 380(6643): 404–409
96. Chen H, Yang J, Cao Q, Wang T, Pu X, He X, Chen X, Li X. π-Interactions suppression of buried interface defects for efficient and stable inverted perovskite solar cells. Nano Energy, 2023, 117: 108883
97. Jung E D, Harit A K, Kim D H, Jang C H, Park J H, Cho S, Song M H, Woo H Y. Multiply charged conjugated polyelectrolytes as a multifunctional interlayer for efficient and scalable perovskite solar cells. Advanced Materials, 2020, 32(30): 2002333
98. Degani M, An Q, Albaladejo-Siguan M, Hofstetter Y J, Cho C, Paulus F, Grancini G, Vaynzof Y. 23.7% efficient inverted perovskite solar cells by dual interfacial modification. Science Advances, 2021, 7(49): eabj7930
99. Rothmann M U, Li W, Zhu Y, Bach U, Spiccia L, Etheridge J, Cheng Y B. Direct observation of intrinsic twin domains in tetragonal $CH_3NH_3PbI_3$. Nature Communications, 2017, 8(1): 14547
100. Thind A S, Luo G, Hachtel J A, Morrell M V, Cho S B, Borisevich A Y, Idrobo J C, Xing Y, Mishra R. Atomic structure and electrical activity of grain boundaries and ruddlesden-popper faults in cesium lead bromide perovskite. Advanced Materials, 2019, 31(4): 1805047
101. Reiche M, Kittler M, Erfurth W, Pippel E, Sklarek K, Blumtritt H, Haehnel A, Uebensee H. On the electronic properties of a single dislocation. Journal of Applied Physics, 2014, 115(19): 194303
102. Cai S, Li Z, Zhang Y, Liu T, Wang P, Ju M G, Pang S, Lau S P, Zeng X C, Zhou Y. Intragrain impurity annihilation for highly efficient and stable perovskite solar cells. Nature Communications, 2024, 15(1): 2329
103. Duan T, Wang W, Cai S, Zhou Y. On-chip light-incorporated *in situ* transmission electron microscopy of metal halide perovskite materials. ACS Energy Letters, 2023, 8(7): 3048–3053
104. You P, Li G, Tang G, Cao J, Yan F. Ultrafast laser-annealing of

perovskite films for efficient perovskite solar cells. Energy & Environmental Science, 2020, 13(4): 1187–1196

105. Zhang Y, Zhou Y. Machine vision for interpreting perovskite grain characteristics. Accounts of Materials Research, 2023, 4(3): 209–211
106. Zhang Y, Zhou Y. Machine learning quantification of grain characteristics for perovskite solar cells. Matter, 2024, 7(1): 255–265
107. Zhou H, Wang K, Nie C, Deng J, Chen Z, Zhang K, Zhao X, Liang J, Huang D, Zhao L, et al. Quantitative analysis of perovskite morphologies employing deep learning framework enables accurate solar cell performance prediction. Small, 2025, 21(18): 2408528
108. Zhang Y, Yu R, Li M, He Z, Dong Y, Xu Z, Wang R, Ma Z, Tan Z. Amphoteric ion bridged buried interface for efficient and stable inverted perovskite solar cells. Advanced Materials, 2024, 36(1): 2310203
109. Orr K W P, Diao J, Dey K, Hameed M, Dubajić M, Gilbert H L, Selby T A, Zelewski S J, Han Y, Fitzsimmons M R, et al. Strain heterogeneity and extended defects in halide perovskite devices. ACS Energy Letters, 2024, 9(6): 3001–3011
110. Hou P, Hu S, Zhang Y, Pan J, Hu M, Chen J, Duan B, Wan L, Lv P, Zhu Y, et al. Ordered self-assembled monolayer improved the buried interface of wide bandgap perovskite for efficient and stable semi-transparent solar cells. Chemical Engineering Journal, 2025, 503: 158499
111. Li Y, Fan H, Xu F, Wang T, Shan C, Li W, Gu X, Lai X, Luo D, Sun Z, et al. High-performance inverted perovskite solar cells enhanced via partial replacement of dimethyl sulfoxide with *N*-methyl-2-pyrrolidinone. Solar RRL, 2022, 6(12): 2200816